Heat transfer enhancement from a small rectangular channel with different surface protrusions by a turbulent cross flow jet

Ashok K. Barik [a], *, Arnab Mukherjee [a], Pandaba Patro [b]

[a] *Mechanical Engineering Department, College of Engineering and Technology (CET), Bhubaneswar 751003, Odisha, India*
[b] *Mechanical Engineering Department, National Institute of Science and Technology (NIST), Berhampur 761008, Odisha, India*

ARTICLE INFO

ABSTRACT

In the present study, thermo-hydrodynamic performance of a small rectangular channel with different protruded surfaces is investigated numerically in a three−dimensional computational domain. An air jet impinging normal to the main flow is considered to enhance heat transfer rate. Conservation equations for mass, momentum and energy are solved using finite volume method with SST $k-\omega$ turbulence model. Three different protrusion shapes have been tested: rectangular, trapezoidal and triangular, respectively. The duct and nozzle Reynolds numbers are varied in the range of $17,831 \leq Re_{Dh,duct} \leq 53,490$ and $5,136 \leq Re_{Dh,nz} \leq 11,980$, respectively. Also, three different nozzle positions ($X/D_{h,duct} = 8.717$, 11.597 and 14.258) along the axial direction of rectangular duct have been considered to choose the best location for heat transfer enhancement. A higher heat transfer enhancement rate is observed at the nozzle position 2 ($X/D_{h,duct} = 11.597$) as compared to the other positions considered in this study. Flow recirculation in inter-protrusion spaces has also been discussed. In this hybrid cooling strategy, the pumping power requirement with protrusions is observed to be higher than that of without protrusions. The heat transfer enhancement rate with triangular protrusions is found to be more as compared to other protrusion shapes.

© 2015 Elsevier Masson SAS. All rights reserved.

1. Introduction

The miniaturization of electronics devices along with the faster operational speed demand effective and new methods to transfer heat to the coolant flowing over the heated surfaces. Generally, the temperature of fluid near the hot wall is always higher than the temperature of fluid in the core region of a channel. Therefore, heat transfer rate will be enhanced if the cold fluid from the core region is carried by some means and mixed with the hot fluid near the wall. In the past, several cooling strategies such as forced convection cooling, jet impingement cooling, fin cooling and the geometrical modification of surfaces by providing different protrusions were employed to augment the heat transfer. For electronics cooling, many researchers [1−3] employed different cooling techniques and provided a comprehensive study on this field.

Heat transfer from the hot wall can be enhanced by putting turbulators of various shapes such as transverse ribs [4,5], W-shaped ribs [6], and V-shaped ribs [7]. The perforated ribs can enhance heat transfer rate significantly by breaking the viscous sub-layer near the wall, which leads to a higher mixing of the hot and cold fluids. The heat transfer enhancement for full and half perforated baffles attached to a hot surface was studied by Karwa et al. [8] and Karwa and Maheshwari [9]. The Nusselt number was increased by 79−169% for fully perforated baffles, whereas for half perforated baffles, it was increased by 133−274%. The thermo hydraulic performance of a turbulent flow through a tube fitted with perforated tube inserts have been investigated by Bhuiya et al. [10]. They found that Nusselt number and friction factor are increased by 110−340% and 110−360%, respectively. In an experimental study, Alam et al. [11] reported that Nusselt number for a perforated V-shaped blockage has been improved by 33% as compared to a solid blockage. Heat transfer enhancement using ribs of different shapes (such as rectangular, trapezoidal and delta) has also been investigated by Zhou and Feng [12]. The thermo hydraulic performance of punch hole-ribs was superior to ribs without punch hole.

It was shown by various investigators [13−18] that the heat transfer augmentation by jet impingement is one of the efficient

* Corresponding author. Tel.: +91 674 2364075; fax: +91 674 2364172.
E-mail addresses: ashokbarik.mech@gmail.com, ashok_iit@hotmail.com (A.K. Barik).

methods, which can dissipate heat more effectively compared to a simple forced convection method. The reason for high heat transfer rate by an impinging jet is attributed to the formation of small-scale vortex pairs and the exchange of momentum between the jet and the surrounding fluid. Moreover, a hybrid heat transfer augmentation method has been adopted by Tan et al. [19] by impinging air jet on a protruded surface. Two different shapes of protrusions (i.e., V-shaped and rectangular) have been employed by them to investigate the heat transfer rate in the Reynolds number range of 6,000 to 30,000. For a same jet Reynolds number, the heat transfer was augmented by 30%, when a smooth wall was replaced with a ribbed wall. The jet impingement heat transfer from triangular and rectangular protruded walls was investigated experimentally by Gau and Lee [20]. They reported that the heat transfer enhancement with the triangular protrusions was better than the rectangular protrusions. In case of the triangular protrusions, the widely opened cavity between the neighboring ribs causes an intense transport of colder fluid into the cavity. Thus, the heat transfer rate is increased. The heat transfer enhancement by different protrusion angles (such as 90°, 60° and 45°) has been studied experimentally by Yan and Mei [21]. They found that the heat transfer enhancement with 45° angle ribs was higher than that of 90° and 60° ribs. The above researchers have concentrated their focus on the ribbed surfaces without taking the account of the cross flow schemes.

Different cross flow schemes for micro grooved surface were investigated by Xing et al. [22]. The best heat transfer performance was attained at the minimum cross flow as demonstrated by them. A similar study was conducted by Su and Chang [23] to study the combined effects of groove and nozzle size distribution on heat transfer enhancement. Liquid Crystal Thermography (LCT) had been implemented by Wang et al. [24] to investigate heat transfer in cross flows. They showed that a more pronounced effect on heat transfer enhancement was found out at a lower velocity ratio. A flow visualization methods had been carried out by Nakabe et al. [25] by using an inclined impinging jet in a cross flow. The heat transfer performance of an array of jet impinging on the dimples has been investigated by Kanokjaruvijit and Martinez-botas [26] using liquid crystal method. They showed that the impingement heat transfer performance was better at larger nozzle distance due to coupled effect of impingement and channel flow. They also reported that the heat transfer rate with the nozzle distance to diameter ratio of 4 was more as compared to other ratios of 2 and 8. However, Gau and Chung [27] showed that the heat transfer is augmented when a plane surface is replaced with the concave and convex surfaces by varying the slot-width to surface diameter ratios in the range of 8−45. Chyu et al. [28] investigated the heat transfer performances for hemispherical and tear-drop shaped dimples. Their results show that the tear-shaped dimples improve the heat transfer rate significantly as compared to the hemispherical dimples; although the pressure drop with the tear-shaped dimples was higher than that of the hemispherical dimples. Furthermore, the flow past a staggered array hemispherical dimples was studied experimentally by Mahmood et al. [29] using the smoke-wire technique. They showed that the vortex shedding mechanism improves the heat transfer rate for dimpled surfaces by the factor of 1.85−2.89 as compared to a flat plate surface. Recently, Wang et al. [30] introduced delta winglet vortex generator pairs (VGP) in the upstream of the nozzle to control the cross-flow effect and jet impingement heat transfer enhancement. They concluded that the VGP configurations augment heat transfer enhancement in the cross-flow by promoting the jet penetration.

From the above discussions, it is clear that the heat transfer enhancement from a protruded surface with cross flow approach has not yet been drawn much attention of researchers. In the present study, therefore, an attempt has been made to investigate the heat transfer augmentation by implementing the above hybrid scheme. The jet position, duct and jet Reynolds number have been varied to study their effects on the heat transfer from a heated surface. The effect of Reynolds number on pumping power has also been discussed.

2. Mathematical formulation

2.1. Physical description and grid arrangement

In the present numerical investigation, a rectangular duct of size 0.67 m × 0.023 m × 0.03 m has been used as shown in Fig. 1. Air enters the inlet of the rectangular duct at velocity, u_{in} and atmospheric temperature, T_{∞}. A square nozzle placed on the top surface of the duct impinges air to the main duct flow so that both the flows will form a cross flow with each other. This will enhance the mixing, and hence, increase the heat transfer rate from the bottom hot surface. Moreover, protrusions of different shapes (i.e., rectangular, trapezoidal and triangular) have also been provided on the bottom hot surface to further augment the heat transfer rate. The physical dimensions for different shapes of the protrusions are shown in Fig. 2. The hot surface (of length X/Dh_{duct} = 5.76) is maintained at a constant temperature (T_w). An extra length of 10 times the hydraulic diameter of the duct has been considered upstream of the hot surface so as to ensure a fully developed flow in the duct. Similarly, an extra length of 11 times the hydraulic diameter is taken in downstream of the hot surface to reduce the effect of backflow at the duct exit. Fig. 3 shows the grid arrangement for the present computational study. The meshes on the duct inlet, nozzle inlet, bottom surface with trapezoidal protrusions and pressure outlet are shown for the sake of clarity. The inlet and outlet surfaces are meshed with triangular cells. The bottom surface except the hot wall is meshed with rectangular cells in order to control the number of cells.

Tetrahedral meshes have been adopted to mesh the hot surface along with the protrusions. Therefore, the total computational domain is meshed with a hybrid meshing scheme (i.e., combination of hexahedral and tetrahedral meshes). An expanded view of the mesh arrangement of nozzle inlet as well as protrusions is shown in Fig. 3(a) and (b), respectively. The hydraulic diameters of the duct and nozzle are 0.026 m and 0.005 m, respectively.

Following assumptions are taken for solving the governing equations:

1. Flow is steady, three-dimensional and turbulent.
2. The working fluid (air) is Newtonian and incompressible.
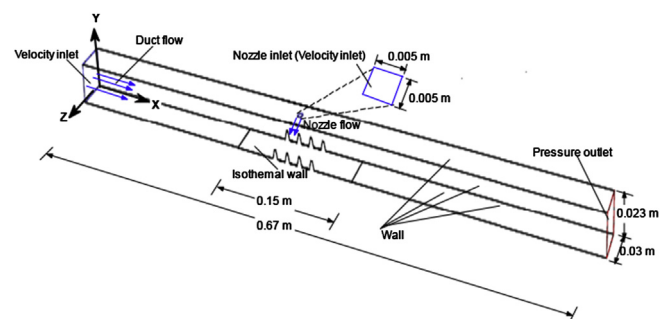3. Fluid properties such as thermal conductivity (λ), dynamic viscosity (μ) are kept constant.

Fig. 1. Schematic diagram of computational domain with different boundary conditions.
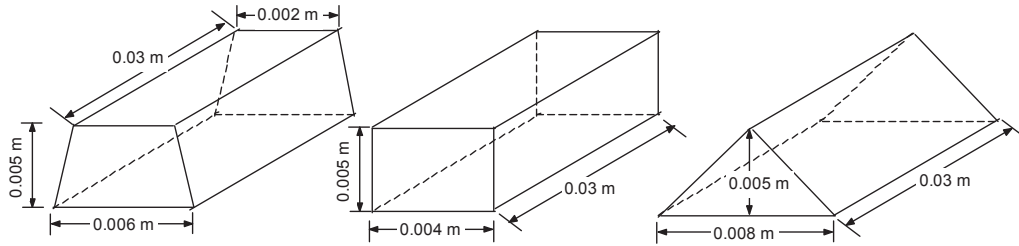
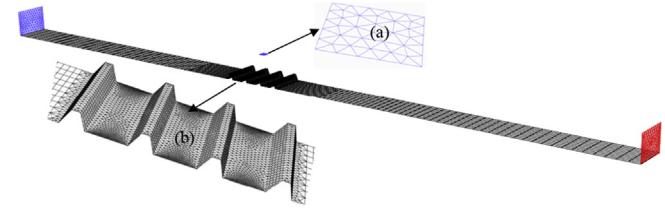**Fig. 2.** Physical dimensions of different protrusion shapes.

Fig. 3. Mesh arrangement of the computational domain with duct inlet, bottom wall and outlet; (a) expanded view of mesh at the nozzle inlet (b) trapezoidal surface protrusions.

2.2. Governing equations

The Reynolds time-averaged equations for mass, momentum, energy in an inertial reference frame are written as follows:

$$Continuity\ equation : \frac{\partial U_i}{\partial x_i} = 0 \tag{1}$$

$$Momentum\ equation : \rho U_j \frac{\partial U_i}{\partial x_j} = -\frac{\partial P}{\partial x_i} + \frac{\partial}{\partial x_j}\left(2\mu S_{ij} - \rho \overline{u_i' u_j'}\right) \tag{2}$$

$$Energy\ equation : \rho U_j \frac{\partial T}{\partial x_j} = \frac{\partial}{\partial x_j}\left(\frac{\lambda}{c_p}\frac{\partial T}{\partial x_j} - \rho \overline{T' u_j}\right) \tag{3}$$

The mean stain rate is defined as:

$$S_{ij} = \frac{1}{2}\left(\frac{\partial U_i}{\partial x_j} + \frac{\partial U_j}{\partial x_i}\right) \tag{4}$$

where μ, λ and c_p represent the dynamic viscosity, thermal conductivity and specific heat at constant pressure for the working fluid. Moreover, P, T, and U_i are the mean pressure, temperature and velocity, respectively. T' and u_i' are the fluctuating temperature and velocity. The Reynolds stress $(-\rho \overline{u_i' u_j'})$ and turbulent heat flux $(-\rho \overline{u_i' T'})$ terms are appeared due to the time averaging; and these terms need to be closed by using the appropriate turbulence model. The Reynolds stress can be specified using a linear eddy viscosity model as follows:

$$-\rho \overline{u_i' u_j'} = 2\mu_t S_{ij} - \frac{2}{3}\rho k \delta_{ij} \tag{5}$$

where, k denotes the turbulent kinetic energy and μ_t represents the eddy viscosity, which are to be specified by solving the transport equations for the turbulent kinetic energy (k) and specific dissipation rate using the $k-\omega$ turbulence model. Similarly, the turbulent heat flux is defined as

$$-\rho \overline{u_i' T'} = \frac{\mu_t}{Pr_t}\frac{\partial \overline{T}}{\partial x_i} \tag{6}$$

Here, Pr_t denotes the turbulent Prandtl number. In the present study, the SST $k-\omega$ turbulence model proposed by Mentor [31] is implemented to model the turbulence quantities. Governing equations for the turbulence kinetic energy (k) and specific dissipation of turbulence kinetic energy (ω) are written as follows:

$$\frac{\partial}{\partial x_i}(\rho k u_i) = \frac{\partial}{\partial x_j}\left[\left(\mu + \frac{\mu_t}{\sigma_k}\right)\frac{\partial k}{\partial x_j}\right] + \min(P_k, 10\rho\beta^* k\omega) - \rho\beta^* k\omega \tag{7}$$

$$\frac{\partial}{\partial x_i}(\rho \omega u_i) = \frac{\partial}{\partial x_j}\left[\left(\mu + \frac{\mu_t}{\sigma_k}\right)\frac{\partial \omega}{\partial x_j}\right] + \frac{\alpha\omega}{k}P_k - \rho\beta\omega^2$$
$$+ 2(1 - F_1)\frac{\rho\sigma_{\omega,2}}{\omega}\frac{\partial k}{\partial x_j}\frac{\partial \omega}{\partial x_j} \tag{8}$$

The eddy viscosity is modeled as:

$$\mu_t = \rho\frac{k}{\omega}\frac{1}{\max\left(\frac{1}{\alpha^*}, \frac{SF_2}{a_1\omega}\right)} \tag{9}$$

The modulus of the mean rate-of-strain tensor S is defined as $\sqrt{(2S_{ij}S_{ij})}$. The turbulent viscosity is damped by the coefficient α^* is given as

$$\alpha^* = \alpha_\infty^* \left(\frac{\alpha_0^* + \frac{Re_t}{R_k}}{1 + \frac{Re_t}{R_k}}\right) \tag{10}$$

In Eq. (10), α_0^* and Re_t are defined as $\alpha_0^* = \beta_i/3$, and $Re_t = (\rho k)/\mu\omega$. The blending functions, F_1 and F_2 are given as $F_1 = \tanh(\phi_1^4)$ and $F_2 = \tanh(\phi_2^2)$, where ϕ_1 and ϕ_2 are given as $\phi_1 = \min[\max(\sqrt{k}/0.09\omega y, 500\mu/\rho y^2 \omega), 4\rho k/\sigma_{\omega,2}D_\omega^+ y^2]$, and $\phi_2 = \max[2\sqrt{k}/0.09\omega y, 500\mu/\rho y^2 \omega]$. In ϕ_1 and ϕ_2 terms, y is the distance to the next surface. The positive portion of cross-diffusion is represented by $D_\omega^+ = \max[2\rho/\sigma_{\omega,2}\ \partial k/\partial x_j\ \partial \omega/\partial x_j, 10^{-10}]$. The production of turbulence kinetic energy is defined as

$$P_k = -\rho \overline{u_i' u_j'}\frac{\partial u_i}{\partial x_i} \tag{11}$$

Since in the present study, the flow is assumed to be incompressible, so the term β^* in equation (7) is equal to β_i^* that is defined as follows

$$\beta_i^* = \beta_\infty^* \left(\frac{4/15 + (Re_t/R_\beta)^4}{1 + (Re_t/R_\beta)^4}\right) \tag{12}$$

Different model constants used in SST $k–\omega$ turbulence model are given as follows:

$\alpha^*_\infty = 1$, $\beta^*_\infty = 0.09$, $\beta_i = 0.072$, $\sigma_{k,1} = 1.176\sigma_{\omega,1} = 2$, $\sigma_{k,2} = 1$, $\sigma_{\omega,2} = 1.168$, $R_k = 6$, $a_1 = 0.31$ and $R_\beta = 8$.

2.3. Boundary conditions

The boundary conditions imposed on the computational domain has been shown in Fig. 1. The velocity inlet boundary conditions have been imposed on nozzle and duct inlets, since air enters the computational domain through these surfaces at uniform velocity. The side and top surfaces (excluding the nozzle inlet) are taken as adiabatic wall. A constant temperature has been imposed on the heated bottom wall. The pressure outlet boundary condition is applied on the outlet because the ambient pressure is prevailed there.

The mathematical descriptions of different boundary conditions are given as follows:

At adiabatic walls:

$$u = v = w = 0, \text{ and } \frac{\partial T}{\partial x} = \frac{\partial T}{\partial y} = \frac{\partial T}{\partial z} = 0 \qquad (13)$$

At solid isothermal wall:

$$u = v = w = 0, \text{ and } T = T_w = 373\,K \qquad (14)$$

$$\text{At duct inlet}: \quad u = u_{in}, T = T_\infty = 300\,K \qquad (15)$$

$$\text{At nozzle inlet}: \quad v = -v_{in}, T = T_\infty = 300\,K \qquad (16)$$

Here u, v and w are the velocity components in the x, y, and z-direction, respectively.

At pressure outlet:

$$p = p_\infty \text{ and } T = T_\infty \qquad (17)$$

where, p_∞ and T_∞ are the ambient pressure and temperature, respectively. The standard wall function as proposed by Launder and Spalding [32] has been used to link the solution variables at near-wall cells to the corresponding quantities on the wall. Similar wall functions have been employed by Jha and Dash [33], Barik et al. [34,35] and Patro and Dash [36] for various applications. The law-of-wall for mean velocity is given as:

$$\frac{U_p k_p^{1/2} c_\mu^{1/4}}{\tau_w/\rho} = \frac{1}{\kappa}\ln(Ey^*) \qquad (18)$$

$$y^* = \frac{\rho k_p^{1/2} c_\mu^{1/4} y_p}{\mu} \qquad (19)$$

where, E denotes the empirical constant equal to 9.793, κ is the von Karman constant having a value 0.4187 and U_p is the mean velocity of fluid at a point 'p'. The turbulent intensity at duct and nozzle inlets are computed as

$$I = 0.016Re^{-1/8} \qquad (20)$$

2.4. Numerical solution procedure

The governing equations for mass, momentum, energy, turbulent kinetic energy (k) and the specific dissipation (ω) are discretized in a three-dimensional computational domain to yield a set of algebraic equations, which are then solved by imposing the boundary conditions with the second order upwind scheme using Ansys-Fluent 16.0. SIMPLE algorithm has been employed for pressure–velocity coupling to solve pressure correction equation. In the present study, the SST $k–\omega$ turbulence model has been used. In the past, it was recommended by various researchers [37–40] to use SST $k–\omega$ model for the prediction of the jet-impingement heat transfer. Moreover, the different variants of turbulence model have been used by Dutta et al. [41] to predict the surface Nusselt number for an impinging jet. They concluded that both standard as well as SST $k–\omega$ models were capable of predicting the surface Nusselt number very well, when the ratio of the jet spacing to the hydraulic diameter of the nozzle was low (i.e., 4 to 4.9). In the present study, this ratio is taken as 4.6. Thus, it is expected that SST $k–\omega$ model may predict the heat transfer quite well.

3. Validation of numerical methodology

The present numerical scheme has been validated with some of the existing experimental data available in the literature. However, the heat transfer augmentation and thermal management of a small rectangular channel with surface protrusions and the cross flow approach is a new research area. Hence, the literature on such a hybrid cooling scheme are not abundant. Nevertheless, the present numerical scheme is validated with Sleicher and Rouse [42] correlation by taking a three-dimensional circular pipe of diameter 0.026 m and length 0.67 m, and applying a uniform wall heat flux (i.e., 100 W/m^2) to the fully developed portion of the duct. This particular problem is chosen, since the boundary conditions for the validation purpose is similar with our present boundary conditions.

A grid sensitivity test has also been carried out for the present validation, and it is found that a grid size of 28,891 cells predicted the surface Nusselt number reasonably well with the above correlation as shown in Fig. 4. However, the Sielder and Tate [43] correlation over predicts the Nusselt number since it is used for the fluids having a temperature dependent properties. As constant fluid properties are used in the present simulation, the computed values of Nusselt number are lower than the values reported by Sielder and Tate [43]. Moreover, the computed values of Nusselt number are closer to the values predicted by Kakac et al. [44] correlation. For the above validation, SIMPLE method has been used for pressure–velocity coupling and the second order upwind scheme
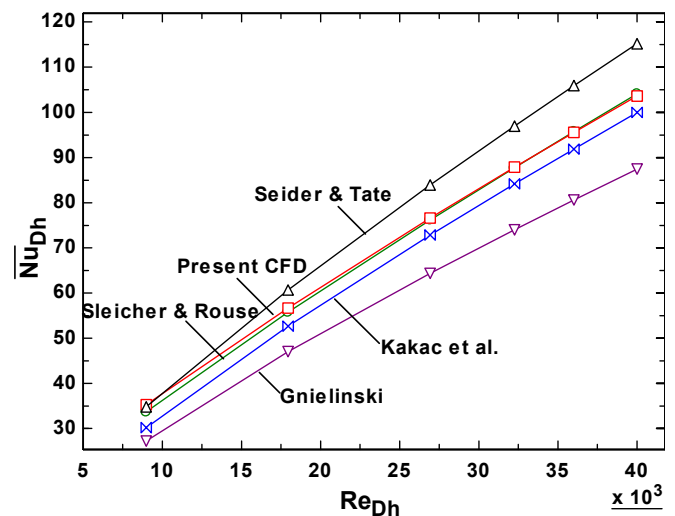

Fig. 4. Variation of average Nusselt number with Reynolds number with uniform wall heat flux.

is used for solving mass, momentum and energy equations. SST $k-\omega$ model has been used for the simulation. From this discussion, it is clear that the present numerical scheme is capable of predicting the surface Nusselt number very well.

4. Results and discussions

4.1. Grid sensitivity test (trapezoidal protrusion)

Fig. 5 shows the grid sensitivity test for the present small rectangular duct with surface protrusions and cross flow impingement. It can be seen that the area weighted average Nusselt number ($\overline{Nu}_{Dh,duct}$) is increased by 2.8% as the number of cells increase from 182,730 to 242,700. The increase in Nusselt number is insignificant (0.03%) on further increasing the numbers of cells. Thus, 242,700 cells are used as a grid independent mesh for obtaining the solution variables in our further simulations. The overall Nusselt number is defined as:

$$\overline{Nu}_{Dh,duct} = \frac{1}{A} \int Nu_{Dh,duct} dA \qquad (21)$$

In Eq. (21), area dA is the wetted area i.e., internal surface area from where heat transfer takes place.

The local Nusselt number is calculated as:

$$Nu_{Dh,duct} = \frac{h_w D_{h,duct}}{k} \qquad (22)$$

where local heat transfer coefficient, $h_w = q_w/T_w - T_b = k(\partial T/\partial y)_{y=0}/T_w - T_b$.

The bulk mean temperature is computed from the local temperature, T according to Eq. (23).

$$T_b = \frac{1}{A} \int T dA \qquad (23)$$

In Eq. (23), area dA is the cross sectional area. All the properties are calculated at bulk mean temperature.

The duct Reynolds number is defined as:

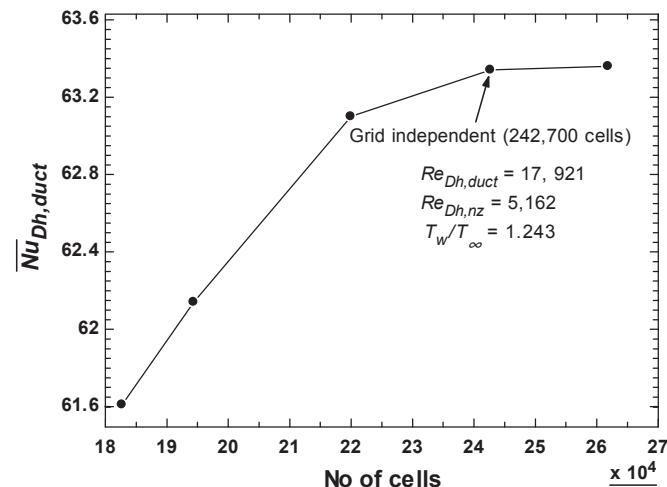$$Re_{Dh,duct} = \frac{\rho u_{in} D_h}{\mu} \qquad (24)$$

where, u_{in} is the velocity of air in the duct, and D_h is the hydraulic diameter of the rectangular duct. Similarly, the Reynolds number of nozzle ($Re_{Dh,nz}$) is calculated using the nozzle inlet velocity and hydraulic diameter of the nozzle.

4.2. Effect of nozzle position on Nusselt number (trapezoidal protrusion)

To investigate the effect of nozzle positions on the heat transfer enhancement, the position of the nozzle impinging normal to the main flow has been varied by considering three different axial locations ($X/D_{h,duct} = 8.72$, 11.59 and 14.25). Fig. 6 shows the variation of area weighted average Nusselt number with duct Reynolds numbers for different nozzle positions. It is evident that the Nusselt number is increased with the duct Reynolds number for all the nozzle placements due to the forced convection effect.

At a particular nozzle Reynolds number, the duct Reynolds number is varied from 17,831 to 53,490. The Nusselt number has been observed to increase linearly with the duct Reynolds number for the different nozzle positions considered in this study. For example, the Nusselt numbers are augmented by 99%, 113% and 109% in the above range of duct Reynolds number for the nozzle positions of 1, 2 and 3, respectively. Thus, it can be noticed that the maximum amount of heat is transferred to the air when the nozzle is placed at the position 2. Expanded views of velocity contours (expanded and cutaway views) are shown in Fig. 7(a)–(c). It is seen from Fig. 7(a) that the duct and nozzle flows are mixed with each other before reaching the protruded surface. The protrusions reduce the cross section of the flow, and consequently the flow is accelerated so that high velocity gradients are seen in the upstream top corner of the protrusion. The flow then finds a sudden expansion in the downstream which leads to a reverse flow because of which a recirculation zone is created. At the nozzle position 3, similar phenomena could be seen as has been shown in Fig. 7(c). Similar explanations have been given by Labbe [45] to study the flow and heat transfer characteristics of a ribbed duct. At nozzle positions 1 and 3, the heat transfer rate is less as compared to that of the nozzle position 2 (i.e., Fig. 6). This is attributed to two reasons: (i) the accelerated flow moves close the adiabatic top wall. Thus, it may not carry more heat from the bottom isothermal wall. (ii) The nozzle at positions 1 and 3 is not able to move the mean flow strongly into the inter protrusion gaps. At position 2, the flow
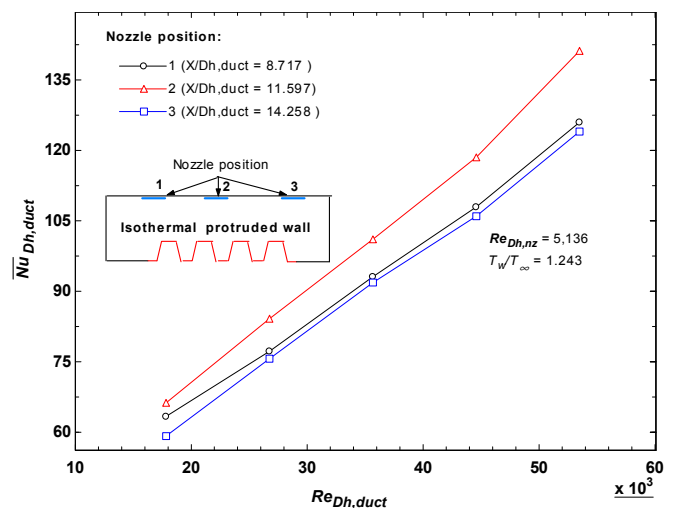

Fig. 5. Effect of number of cells on area weighted average Nusselt number ($\overline{Nu}_{Dh,duct}$).

Fig. 6. Variation of the average Nusselt number of an isothermal surface with the duct Reynolds number ($Re_{Dh,duct}$) as a function of nozzle position.
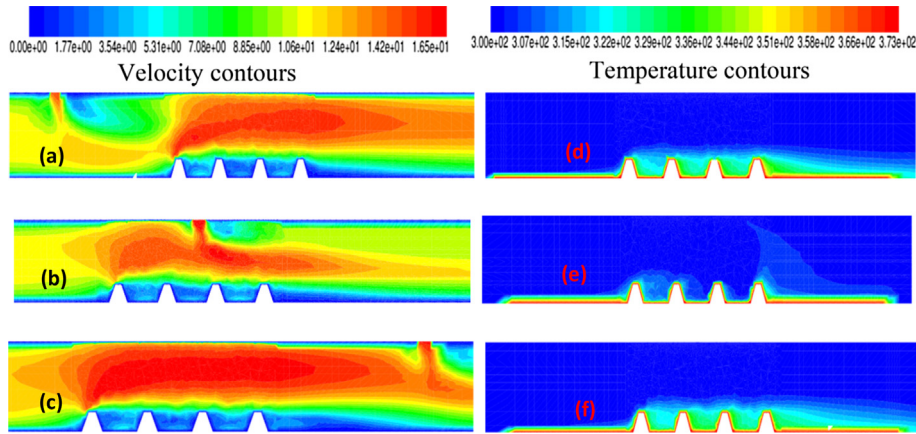
Fig. 7. Expanded and cutaway views of velocity contours ((a), (b), (c)) and temperature contours ((d), (e), (f)) in $X-Y$ plane passing through vertical the midsection of the duct at $Re_{Dh,duct} = 17{,}831$, and $Re_{Dh,nz} = 5{,}136$: (a), (d) nozzle position 1; (b), (e) nozzle position 2; (c), (f) nozzle position 3.

from the nozzle is directly impinged into the inter protrusion gaps (i.e., Fig. 7(b)). Therefore, the velocity at inter protrusion gaps and near the heated surface is relatively higher. As a result, the fresh air in contact with the hot surface can dissipate more heat, and therefore, the Nusselt number is higher as compared to other positions (1 and 3). A higher heat transfer augmentation is obtained at nozzle position 2 among all the positions considered. Therefore, the nozzle position 2 is chosen for our further studies. The expanded views of temperature contours are shown in Fig. 7(d)–(f) for different nozzle placements. It can be seen that the temperature of the hot protruded surface is relatively lower at nozzle position 2 as compared to other positions. Moreover, the temperature distribution on the isothermal surface becomes uniform by reducing the local thermal hotspots which is mostly required for any electronic devices.

4.3. Effect of nozzle Reynolds number on Nusselt number as function of duct Reynolds number (trapezoidal protrusion)

Fig. 8 illustrates the effect of the nozzle Reynolds number on the area weighted average Nusselt number for different values of duct Reynolds number. At lower duct Reynolds numbers (i.e., $Re_{Dh,duct} = 8{,}915$ and $17{,}831$), the Nusselt number has been

improved by 36.4% and 21.3%, when the nozzle Reynolds number ($Re_{Dh,nz}$) is increased from 6847 to 11,983. Furthermore, the Nusselt number is increased with duct Reynolds number at a particular nozzle Reynolds number. For example, at $Re_{Dh,nz} = 6{,}847$, the Nusselt number has been improved by 114.5% as duct Reynolds number ($Re_{Dh,duct}$) is increased from 8915 to 44,577, which clearly signifies the dependency of the Nusselt number on the duct Reynolds number.

However, the Nusselt number is increased by 4.6%, 3.5% and 2.1% for duct Reynolds number of 26,746, 35,661 and 44,577, respectively on the higher side as the nozzle Reynolds number is varied. Therefore, the effects of the variations in nozzle Reynolds number are not felt on the heat transfer augmentation, although the value of the Nusselt number at a higher duct Reynolds number is high. This is due to the fact that the high momentum of the duct flow (at high duct Reynolds number) blows the low momentum fluid from the jet. Thus, the low momentum jet fluid is not able to reach the hot protruded surface to carry the heat from it. So, the variations in Nusselt number with nozzle Reynolds number (i.e., Fig. 8) are almost flat in nature at higher Reynolds number.

At particular nozzle Reynolds number, the value of the Nusselt number is higher at high duct Reynolds number than that of the value obtained at low duct Reynolds number as shown in Fig. 8. This fact is attributed to the strong forced convection of the duct flow, which can produce a rapid bodily motion of the fluid so as to enhance the heat transfer. At $Re_{Dh,nz} = 6{,}847$, the turbulent kinetic energy contour maps (flooded with color (in the web version)) are shown in Fig. 9(a)–(d) for different duct Reynolds numbers. In Fig. 9(a), it is seen that the nozzle fluid touches the bottom hot surface, and thus, the heat from bottom isothermal surface is transferred by the combined convective effect of the main fluid as well the jet fluid. However, it is quite obvious from Fig. 9(b) that the nozzle fluid is blown with the main flow as the duct Reynolds number is increased. An intense blow off of the nozzle fluid is seen (Fig. 9(c)–(d)) on further increasing the duct Reynolds number. Therefore, it is evident that the nozzle flow is blown away by the high momentum of the main flow without reaching the hot surface for higher duct Reynolds number.

The variation of centerline turbulence kinetic energy at different nozzle Reynolds number for a particular duct Reynolds number (i.e., $Re_{Dh,duct} = 8{,}915$) is shown in Fig. 10. A higher centerline turbulence kinetic energy is obtained at the impingement point as nozzle Reynolds is increased for lower duct Reynolds number. This reason for the increase in turbulent kinetic energy has already been discussed.
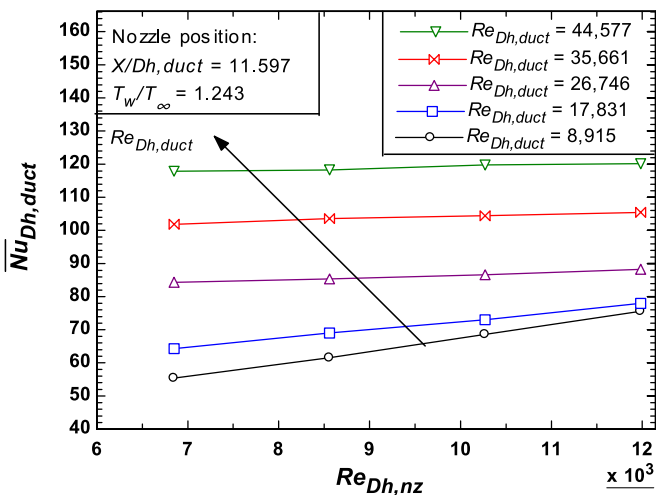

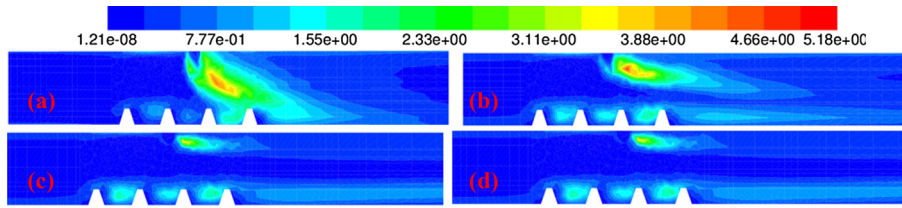**Fig. 8.** Average Nusselt number variation with nozzle Reynolds number.

Fig. 9. Expanded and cutaway views of turbulent kinetic energy in X—Y plane at $Re_{Dh,nz} = 6,847$ and (a) $Re_{Dh,duct} = 8,915$; (b) $Re_{Dh,duct} = 17,831$; (c) $Re_{Dh,duct} = 35,661$; (d) $Re_{Dh,duct} = 44,577$.
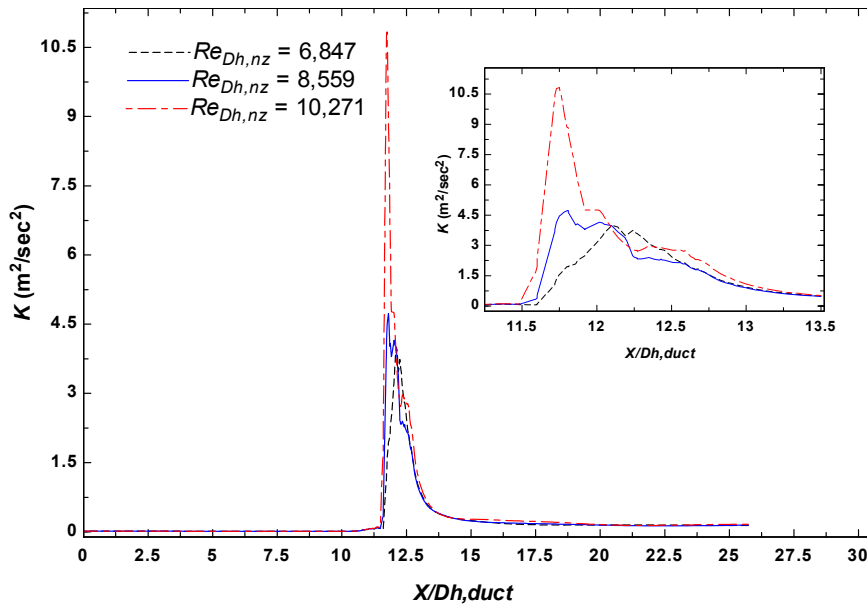

Fig. 10. Variation of duct centerline turbulence kinetic energy at different nozzle Reynolds number for $Re_{Dh,duct} = 8915$.

4.4. Effect of duct Reynolds number on pumping power as function of nozzle Reynolds number (trapezoidal protrusion)

For economic design of any electronic cooling system, it is vital to investigate the effect of the duct Reynolds number on pumping power as well as pressure drop. Selection of a new cooling methodology depends not only on the heat transfer enhancement, but also on the pumping power requirement. Thus, effect of duct Reynolds number on pumping power and pressure drop has been

depicted in Fig. 11(a)—(b). For above investigation, the nozzle placed at position 2 to impinge air on the isothermal surface having trapezoidal protrusions mounted over it. The pumping power is calculated as follows:

$$\text{Pumping power } (pp) = \dot{Q}_{total} \times \Delta p \qquad (25)$$

In Eq. (25), $\dot{Q}_{total}$ is the total volume flow rate in the rectangular duct, which is the sum of the volume flow rates through inlets of
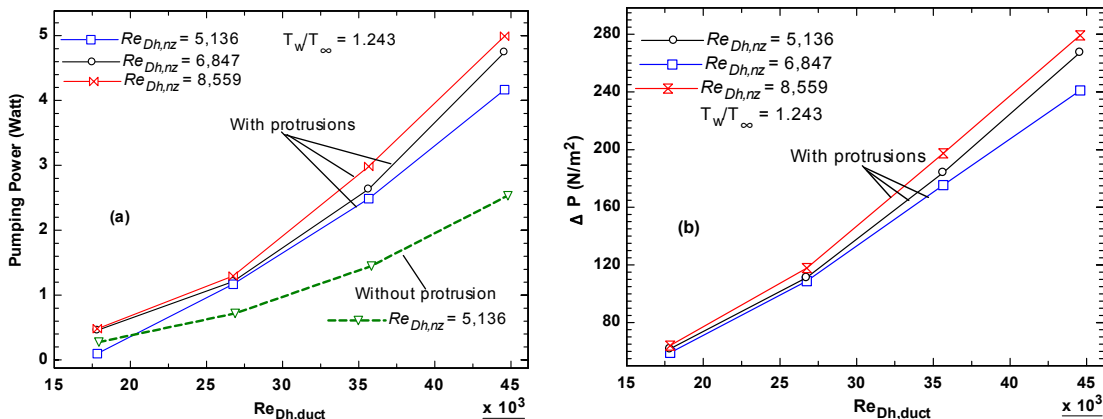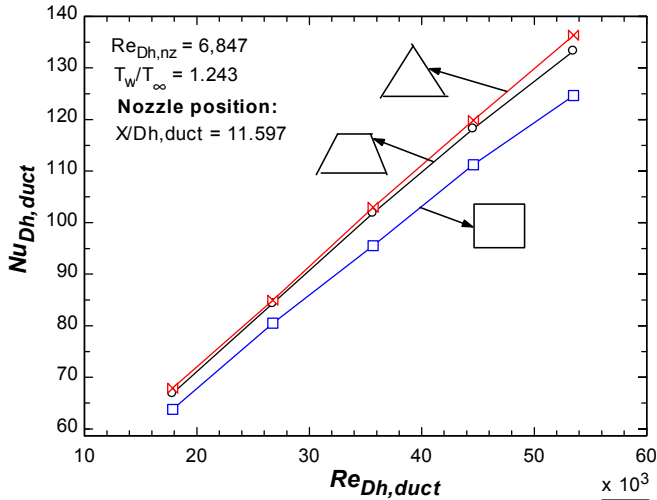

Fig. 11. Variation of (a) pumping power; (b) pressure drop with duct Reynolds number.
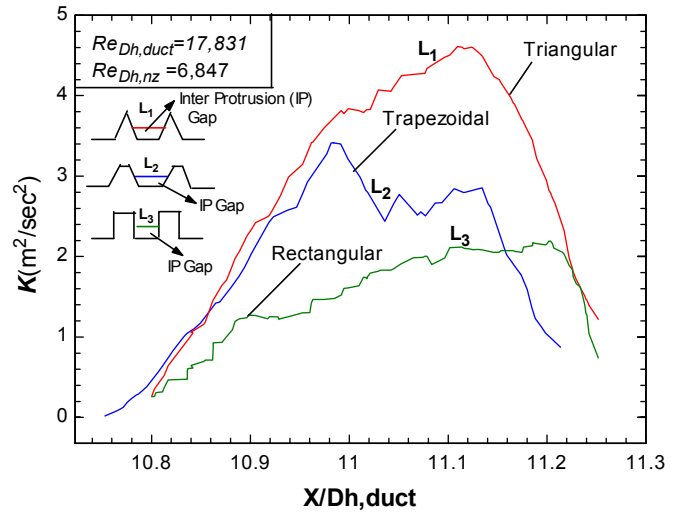
Fig. 12. Average Nusselt number variation with duct Reynolds number for different surface protrusion shapes.

Fig. 14. Variation of turbulent kinetic energy with inter-protrusion axial distance.

the duct and nozzle. The pressure drop (Δp) is calculated by taking the difference of inlets (nozzle and duct) and outlet pressures. As it is expected, the pumping power is noticed to increase with the duct Reynolds number for a particular nozzle Reynolds number.

A higher pressure drop is obtained at a higher duct Reynolds number which has been shown in Fig. 11(b). Moreover, the volume flow rate is increased at a higher duct Reynolds number. Therefore, the combined effect of increased pressure drop and volume flow rate causes the pumping power to increase. It is also noticed that the pumping power significantly is increased when surface protrusions are mounted over the bottom surface. It can be seen that for a same duct as well as nozzle Reynolds numbers (i.e., $Re_{Dh,nz} = 5,136$ and $Re_{Dh,duct} = 44,577$), the pumping power is increased from 2.55 W to 4.15 W. The above values of pumping power may be practically viable for electronics cooling system. The electronic device needs to be operated at a lower duct Reynolds number to keep the pumping power requirement at a minimum level. However, the effects height and pitch of surface protrusions along the use of multiple nozzles need to be further investigated.

4.5. Effect of shape of surface protrusion on heat transfer rate

Fig. 12 shows the variation of the Nusselt number (based on the area weighted average) with the duct Reynolds number for

different shapes of surface protrusions considered in this work. It is evident that the Nusselt number, and thus, the heat transfer from the heated surface have been enhanced with the duct Reynolds number for a particular value of the nozzle Reynolds number. For example, the Nusselt number has been increased by 99% when the duct Reynolds is increased from 17,830 to 53,490 for trapezoidal surface protrusions. Also, the heat transfer rate is improved with the geometrical shapes of the protrusions. At $Re_{Dh,duct} = 53,490$, the heat transfer rate is enhanced by 10%, when rectangular protrusions are replaced with the triangular protrusions of same cross sectional area. Therefore, the geometrical shape has been considered as the third best parameter to influence the heat transfer rate. The heat transfer rate with triangular protrusion is higher as compared to other shapes (Fig. 12) because a higher mean turbulence kinetic energy have been generated in the main flow as well as inter protrusion gaps. The generation of mean turbulence kinetic energy in the main flow has been depicted in Fig. 13(a)–(c) in terms of turbulent kinetic energy contours. It is quite clear that the mean turbulent kinetic energy is found to be higher with the triangular protrusions as shown in Fig. 13(c). The turbulent kinetic energy is little higher near the nozzle exit due to the mixing of the duct as well as the nozzle flows. For different shapes of the protrusions, the mean turbulent kinetic energy in the inter protrusion gaps has been illustrated in Fig. 14. Three different lines (L₁−L₃) are drawn in the
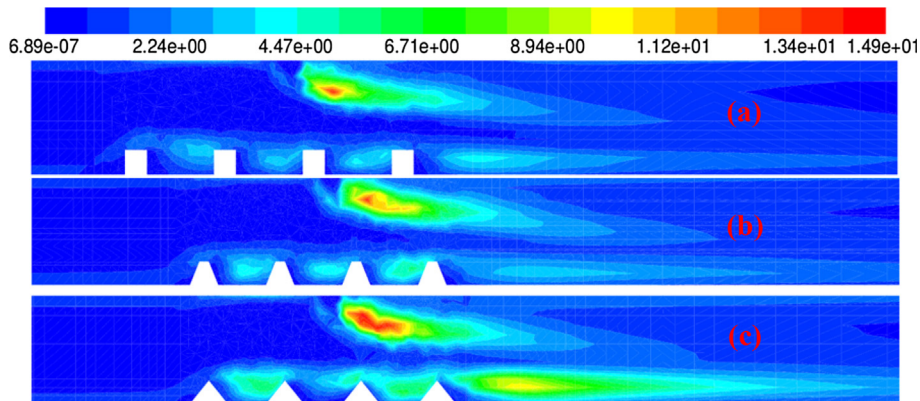
Fig. 13. Contours of turbulent kinetic energy for different surface protrusion shapes at $Re_{Dh,nz} = 6,847$ and $Re_{Dh,duct} = 17,831$: (a) rectangular; (b) trapezoidal and (c) triangular shapes.
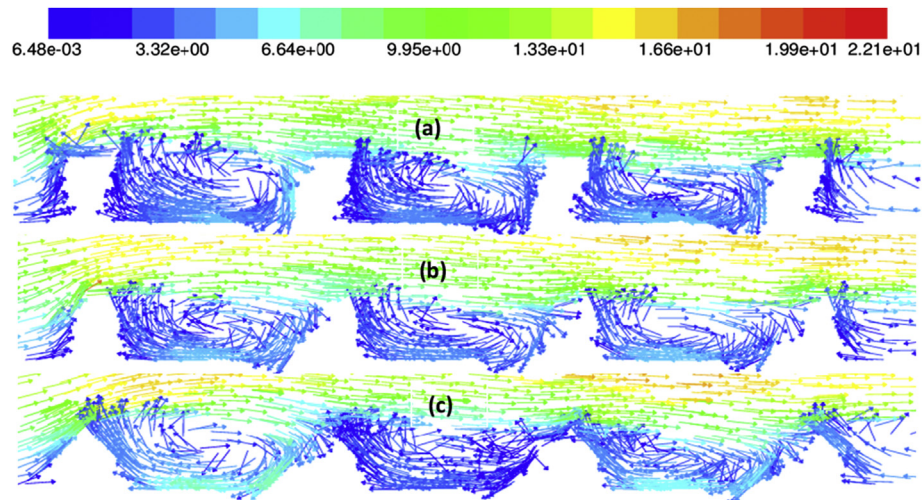
Fig. 15. Expanded and cutaway views of inter-protrusion velocity vectors at $Re_{Dh,nz} = 6847$, and $Re_{Dh,duct} = 17{,}831$: (a) rectangular; (b) trapezoidal and (c) triangular shapes.

inter protrusion gaps so as to quantify the variation of the turbulent kinetic energy along the axial distance as has been shown in Fig. 14. It has been observed that the highest turbulent kinetic energy is produced by the triangular protrusions among all the protrusions considered. Moreover, this argument has been supplemented by the turbulent kinetic energy contour plots as shown in Fig. 13(a)–(c). For triangular protrusions, the higher turbulent kinetic energy is attributed to the presence of the sharp corners which causes inter-protrusion flow recirculation in the inter protrusion gaps. Thus, an enhanced heat transfer is obtained for triangular protrusions.

The inter protrusion recirculation has been shown in Fig. 15(a)–(c). In case of triangular protrusions, the size of the inter-protrusion recirculation bubbles is found to be larger and more intense (i.e., the higher velocity magnitude in the inter protrusion gaps can be seen from the color code (in the web version) of Fig. 15(c)); so that the fluid from the main flow can be drawn rigorously at higher momentum into these regions to enhance the heat transfer rate. Since a low turbulence level is generated in the main flow as well as in between the protrusions (Fig. 13(a)–(b), and Fig. 14), the heat transfer rate for trapezoidal and rectangular protrusions is lower than the triangular protrusions.

Moreover, it is noticed from Fig. 13(a)–(c) that the size of the recirculation zone in the downstream of the last protrusions is increased, when rectangular protrusions are replaced by the triangular protrusions. It has been demonstrated by Han [46] that rib separation is an important parameter having a dominating effect on thermal performance of a surface mounted with parallel ribs. Later on, the convective heat transfer from a rectangular duct has been investigated experimentally and numerically by Wong et al. [47] using cross ribs in turbulent regime. They reported that the geometry of the ribs have significant effect on heat transfer rate since the presence of the ribs directly affect the flow separation in between the ribs. In an experimental investigation of forced convection heat transfer for the ribbed duct, Promvonge and Thinanpong [48] reported that the heat transfer with triangular ribbed surfaces was higher that other shapes of ribs such as wedge and rectangular ribs when the triangular ribs were arranged in staggered manner.

5. Conclusions

Turbulent heat transfer and fluid flow characteristics have been investigated for a protruded isothermal surface by solving Reynolds Averaged Navier Stokes (RANS) equations with the SST $k-\omega$ model. The combined effects of forced convection and jet impingement heat transfer have been investigated by varying duct as well as nozzle Reynolds numbers. The effect of nozzle position and the geometrical shape of different protrusions are also discussed. The major findings of the present study are summarized below:

I. The nozzle position 2 (i.e., $X/D_{h,duct} = 11.59$) is found to be the best location to transfer more heat from the surface as compared to other nozzle positions. This is attributed to a higher turbulence level at this position. At a particular Reynolds number ($Re_{Dh,nz} = 5{,}136$) and position of the nozzle (say, position 2), the Nusselt number is increased by 113%, when the duct Reynolds number is changed from 17,831 to 53,490.

II. The nozzle Reynolds number is found to a second best parameter for the heat transfer enhancement in cross flow cooling strategies. It is observed that the average Nusselt number is increased with the nozzle Reynolds number.

III. The pressure drop, and so the pumping power are increased with the duct Reynolds number. At a particular value of the duct as well as the nozzle Reynolds number, the heat transfer enhancement with triangular protrusions is found to be more than other shapes of protrusions considered.

IV. A strong flow recirculation in the inter-protrusion spaces is observed when triangular nozzles are used. Also, the recirculation bubble size in the downstream of the protruded surface is bigger in size as compared to other protrusion shapes when triangular protrusions are deployed.

Nomenclature

$D_{h,duct}$	hydraulic diameter of duct (m)
I	turbulence intensity
k	turbulent kinetic energy (m^2/s^2)
$\overline{Nu}_{Dh,duct}$	average Nusselt number
$Nu_{Dh,duct}$	local Nusselt number
r	transverse position (Y and Z)
$Re_{Dh,duct}$	reynolds number based on hydraulic diameter of duct
$Re_{Dh,nz}$	Reynolds number based on hydraulic diameter of rectangular nozzle
T_∞	ambient temperature (K)
T_w	isothermal wall temperature (K)
u_{in}	velocity at duct inlet (m/s)

q_w	heat flux of isothermal surface (W/m²)
$\dot{Q}_{total}$	total volume flow rate (m³/s)
T_b	bulk mean temperature (K)
X	axial direction along isothermal surface (m)

Greek letters

Δp	pressure drop (Pa)
λ	thermal conductivity (W/m-K)
μ	dynamic viscosity of fluid (kg/m s)
ρ	fluid density (kg/m³)
ω	specific dissipation rate (1/s)

Subscripts

in	inlet
nz	nozzle
$duct$	duct
w	wall
∞	ambient

References

[1] I. Mudawar, Assessment of high-heat-flux thermal management schemes, Proc. Seventh Intersoc. Conf. Therm. Therm. Mech. Phenom. Electron. Syst. 1 (2000) 1−20.

[2] L.T. Yeh, Review of heat transfer technologies in electronic equipment, ASME J. Electron. Packag. 117 (1995) 333−339.

[3] A. Dewan, P. Patro, I. Khan, P. Mahanta, The effect of fin spacing and material on the performance of a heat sink with circular pin fins, J. Power Energy 224 (2010) 35−46.

[4] B.N. Prasad, J.S. Saini, Effect of artificial roughness on heat transfer and friction factor in a solar air heater, Sol. Energy 41 (1988) 555−560.

[5] D. Gupta, S.C. Solanki, J.S. Saini, Heat and fluid flow in rectangular solar air heater duct having transverse rib roughness on absorber plates, Sol. Energy 51 (1993) 31−37.

[6] A. Lanjewar, J.L. Bhagoria, R.M. Sarviya, Heat transfer and friction in solar air heater duct with W-shaped rib roughness on absorber plate, Energy 36 (2011) 4531−4541.

[7] A.M. Ebrahim Momin, J. Saini, S. Solanki, Heat transfer and friction in solar air heater duct with V-shaped rib roughness on absorber plate, Int. J. Heat Mass Transf. 45 (2002) 3383−3396.

[8] R. Karwa, B.K. Maheshwari, N. Karwa, Experimental study of heat transfer enhancement in an asymmetrically heated rectangular duct with perforated baffles, Int. Commun. Heat Mass Transf. 32 (2005) 275−284.

[9] R. Karwa, B.K. Maheshwari, Heat transfer and friction in an asymmetrically heated rectangular duct with half and fully perforated baffles at different pitches, Int. Commun. Heat Mass Transf. 36 (2009) 264−268.

[10] M.M.K. Bhuiya, M.S.U. Chowdhury, M.T. Saha, Islam heat transfer and friction factor characteristics in turbulent flow through a tube fitted with perforated twisted tape inserts, Int. Commun. Heat Mass Transf. 46 (2013) 49−57.

[11] T. Alam, R.P. Saini, J.S. Saini, Experimental investigation on heat transfer enhancement due to V-shaped perforated blocks in a rectangular duct of solar air heater, Energy Convers. Manage. 81 (2014) 374−383.

[12] G. Zhou, Z. Feng, Experimental investigations of heat transfer enhancement by plane and curved winglet type vortex generators with punched holes, Int. J. Therm. Sci. 78 (2014) 26−35.

[13] J. Sakakibara, K. Hishida, M. Maeda, Vortex structure and heat transfer in the stagnation region of an impinging plane jet, Int. J. Heat Mass Transf. 40 (1997) 3163−3176.

[14] R. Gardon, J.C. Akfirat, The role of turbulence in determining the heat transfer characteristics of impinging jets, Int. J. Heat Mass Transf. 8 (1965) 1261−1272.

[15] N. Didden, C.M. Ho, Unsteady separation in a boundary layer produced by an impinging jet, J. Fluid Mech. 160 (1985) 235−256.

[16] J. Gauntner, N.B. Livingood, P. Hrycak, Survey of Literature on Flow Characteristics of a Single Turbulent Jet Impinging on a Flat Plate, NASA, TN D-5652, Lewis Research Center, USA, 1970.

[17] C.M. Ho, N.S. Nosseir, Dynamics of an impinging jet, part 1: the feedback phenomenon, J. Fluid Mech. 105 (1981) 119−142.

[18] K. Jambunathan, E. Lai, M.A. Moss, B.L. Button, A review of heat transfer data for single circular jet impingement, Int. J. Heat Fluid Flow 13 (1992) 106−115.

[19] L. Tan, J. Zhang, H. Xu, Jet impingement on a rib-roughened wall inside semi-confined channel, Int. J. Therm. Sci. 86 (2014) 210−218.

[20] C. Gau, I.C. Lee, Flow and impingement cooling heat transfer along triangular rib-roughened walls, Int. J. Heat Mass Transf. 43 (2000) 4405−4418.

[21] W.M. Yan, S.C. Mei, Measurement of detailed heat transfer along rib roughened surface under arrays of impinging elliptic jets, Int. J. Heat Mass Transf. 49 (2006) 159−170.

[22] Y. Xing, S. Spring, B. Weigand, Experimental and numerical investigation of impingement heat transfer on a flat and micro-rib roughened plate with different cross flow schemes, Int. J. Therm. Sci. 50 (2011) 1293−1307.

[23] L.M. Su, S.W. Chang, Detailed heat transfer measurements of impinging jet arrays issued from grooved surfaces, Int. J. Therm. Sci. 41 (2002) 823−841.

[24] L. Wang, B. Sundén, A. Borg, H. Abrahamsson, Control of jet impingement heat transfer in cross flow by using a rib, Int. J. Heat Mass Transf. 54 (2011) 4157−4166.

[25] K. Nakabe, K. Inaoka, T. Ai, K. Suzuki, Flow visualization of longitudinal vortices induced by an inclined impinging jet in a cross flow for effective cooling of high temperature gas turbine blades, Energy Convers. Manage. 38 (1997) 1145−1153.

[26] K. Kanokjaruvijit, R.F. Martinez-botas, Jet impingement on a dimpled surface with different cross flow schemes, Int. J. Heat Mass Transf. 48 (2005) 161−170.

[27] C. Gau, C.M. Chung, Surface curvature effect on slot-air jet impingement cooling flow and heat transfer process, J. Heat Transf. 113 (1991) 858−864.

[28] M.K. Chyu, Y. Yu, H. Ding, J.P. Downs, F.O. Soechting, Concavity enhanced heat transfer in an internal cooling passage, ASME Paper, 97-GT-437.

[29] G.I. Mahmood, M.L. Hill, D.L. Nelson, P.M. Ligrani, Local heat transfer and flow structure on and above a dimpled surface in a channel, in: ASME International Gas Turbine and Aero Engine Congress and Exhibition, Germany, May 8−11, 2000.

[30] C. Wang, L. Wang, B. Sundén, A novel control of jet impingement heat transfer in cross-flow by a vortex generator pair, Int. J. Heat Mass Transf. 88 (2015) 82−90.

[31] F.R. Menter, Two-equation eddy-viscosity turbulence models for engineering applications, AIAA J. 32 (1994) 1598−1605.

[32] B.E. Launder, D.B. Spalding, The numerical computation of turbulent flows, Comp. Meth. Appl. Mech. Eng. 3 (1974) 269−2879.

[33] P.K. Jha, S.K. Dash, Employment of different turbulence models to the design of optimum steel flows in a tundish, Int. J. Numer. Methods Heat Fluid Flow 14 (2004) 953−979.

[34] A.K. Barik, S.K. Dash, A. Guha, Experimental and numerical investigation of air entrainment into an infrared suppression device, Appl. Therm. Eng. 75 (2015) 33−44.

[35] A.K. Barik, S.K. Dash, A. Guha, New correlation for prediction of air entrainment into an infrared suppression (IRS) device, Appl. Ocean Res. 47 (2014) 303−312.

[36] P. Patro, S. Dash, Computations of particle-laden turbulent jet flows based on Eulerian model, ASME J. Fluids Eng. 136 (2014) 011301, 1−16.

[37] M.A.R. Sharif, K.K. Mothe, Evaluation of turbulence models in the prediction of heat transfer due to slot jet impingement on plane and concave surfaces, Numer. Heat Transf. Part B 55 (2009) 273−294.

[38] N. Zuckerman, N. Lior, Impingement heat transfer: correlations and numerical modeling, ASME J. Heat Transf. 127 (2005) 544−552.

[39] A.G. Rao, M.K. Belinkov, V. Krapp, Y. Levy, Heat transfer investigations in multiple impinging jets at low Reynolds number, in: ASME GT2010−22720, 2010.

[40] M.L. Paz, B.A. Jubran, A numerical study of an impingement array inside a three dimensional turbine vane, in: ASME GT2010−22270, 2010.

[41] R. Dutta, A. Dewan, B. Srinivasan, Comparison of various integration to wall (ITW) RANS models for predicting turbulent slot jet impingement heat transfer, Int. J. Heat Mass Transf. 65 (2013) 750−764.

[42] C.A. Slicher, M.W. Rouse, A convenient correlation for heat transfer to constant and variable property fluids in turbulent pipe flow, Int. J. Heat Mass Transf. 18 (1975) 677−683.

[43] E.N. Sieder, G.E. Tate, Heat transfer and pressure drop of liquids in tubes, Ind. Eng. Chem. 28 (1936) 1429−1436.

[44] S. Kakac, R.K. Shah, W. Aung, Handbook of Single-phase Convective Heat Transfer, John Wiley and Sons, NewYork, 1987.

[45] O. Labbe, Large-eddy-simulation of flow and heat transfer in ribbed duct, Comput. Fluids 76 (2013) 23−32.

[46] J.C. Han, Square channels with parallel, crossed, and V-shaped angled rib, J. Heat Transf. 113 (1991) 590−596.

[47] T.T. Wong, C.W. Leung, Z.Y. Li, W.Q. Tao, Turbulent convection of air-cooled rectangular duct with surface-mounted cross-ribs, Int. J. Heat Mass Transf. 46 (2003) 4629−4638.

[48] P. Promvonge, C. Thianpong, Thermal performance assessment of turbulent flows over different shaped ribs, Int. Commun. Heat Mass Transf. 35 (2008) 1327−1334.